International Journal of Biological Macromolecules 210 (2022) 565–578

Contents lists available at ScienceDirect

International Journal of Biological Macromolecules

journal homepage: www.elsevier.com/locate/ijbiomac

Hybrid PEGylated chitosan/PLGA nanoparticles designed as pH-responsive vehicles to promote intracellular drug delivery and cancer chemotherapy

Sheng-Jyun Huang [a], Tzu-Hao Wang [a], Ya-Hsuan Chou [a], Hui-Min David Wang [b], Tsai-Ching Hsu [c,e,f], Jia-Le Yow [c], Bor-Show Tzang [c,d,e,f,*], Wen-Hsuan Chiang [a,**]

[a] Department of Chemical Engineering, National Chung Hsing University, Taichung 402, Taiwan
[b] Graduate Institute of Biomedical Engineering, National Chung Hsing University, Taichung 402, Taiwan
[c] Institute of Medicine, Chung Shan Medical University, Taichung 402, Taiwan
[d] Department of Biochemistry, School of Medicine, Chung Shan Medical University, Taichung 402, Taiwan
[e] Immunology Research Center, Chung Shan Medical University, Taichung 402, Taiwan
[f] Clinical Laboratory, Chung Shan Medical University Hospital, Taichung 402, Taiwan

ARTICLE INFO

Keywords:
Acidity-responsive nanovehicles
PEGylated chitosan
cancer chemotherapy

ABSTRACT

To achieve effective intracellular anticancer drug release for boosted antitumor efficacy, the acidity-responsive nanovehicles for doxorubicin (DOX) delivery were fabricated by tailor-made *co*-assembly of amphiphilic PEGylated chitosan$_{20k}$ and hydrophobic poly(lactic-*co*-glycolic acid) (PLGA) segments at pH 8.5. The attained DOX-loaded PEGylated chitosan$_{20k}$/PLGA nanoparticles (DOX-PC$_{20k}$PNs) were characterized to have a spherical shape composed of drug-encapsulated chitosan$_{20k}$/PLGA-constituted solid core surrounded by hydrophilic PEG shells. Compared to non-pH-sensitive DOX-loaded PLGA nanoparticles (DOX-PNs), the DOX-PC$_{20k}$PNs displayed outstanding colloidal stability under serum-containing condition and tended to swell in weak acidic milieu upon increased protonation of chitosan$_{20k}$ within hybrid cores, thus accelerating drug release. The in vitro cellular uptake and cytotoxicity studies revealed that the DOX-PC$_{20k}$PNs after being endocytosed by prostate TRAMP-C1 cancer cells rapidly liberated drug, thus promoting drug accumulation in nuclei to enhance anticancer potency. Moreover, the hydrated PEG shells of DOX-PC$_{20k}$PNs remarkably reduced their uptake by macrophage-like RAW264.7 cells. Importantly, in vivo animal findings showed that the DOX-PC$_{20k}$PNs exhibited the capability of inhibiting TRAMP-C1 tumor growth superior to free hydrophobic DOX molecules and DOX-PNs, demonstrating the great potential in cancer chemotherapy.

1. Introduction

Over the past several decades, chemotherapy has been extensively utilized in the cancer treatment [1–8]. The anticancer drugs such as doxorubicin (DOX) that can suppress the biosynthesis of RNA and DNA have been regularly employed in the clinic for many years [9,10]. Unfortunately, DOX shows several drawbacks when used directly in vivo including short blood circulation time, lack of tumor targeting, life-threating cardiotoxicity, and multi-drug resistance of cancer cells [11,12]. To address the above issues, a varied of polymeric nanoparticles such as polymeric micelles [1–3], polymersomes [4,5] and nanogels [6,7] have been developed as DOX vehicles. These studies showed that the functionalized DOX-carrying polymeric nanoparticles well controlled drug release in response to external stimuli and were selectively accumulated within tumor sites through the innate enhanced permeability and retention (EPR) effect of tumor tissues and/or active tumor targeting, thus promoting intratumoral drug concentration to boost antitumor efficacy [1–7]. However, the preparation of aforementioned drug delivery systems involved the synthesis of complicated materials and use of non-biodegradable materials, thus largely limiting their practical clinical applications. In order to further realize the clinical uses of polymeric nanoparticles-based drug delivery systems in cancer treatment, poly (D,L-lactic-*co*-glycolic acid) (PLGA), a biocompatible and biodegradable polymer, approved by the United States Food and Drug Administration for clinical use, has been widely employed as major component of drug carriers [13–18]. As reported by many

* Correspondence to: B.-S. Tzang, Institute of Medicine, Chung Shan Medical University, Taichung 402, Taiwan.
** Corresponding author.
E-mail addresses: bstzang@csmu.edu.tw (B.-S. Tzang), whchiang@dragon.nchu.edu.tw (W.-H. Chiang).

https://doi.org/10.1016/j.ijbiomac.2022.04.209
Received 11 March 2022; Received in revised form 19 April 2022; Accepted 27 April 2022
Available online 2 May 2022

literatures [13–18], the PLGA-constituted nanoparticles effectively delivered various chemotherapeutic agents (especially hydrophobic drugs) to the tumor sites. Also, the PLGA-based nanoparticles could be degraded by hydrolysis of ester bond linkages in the polymer backbone. Lactic acid and glycolic acid, which are biocompatible and rapidly eliminated from the body via the renal system, are the end products of degradation [17]. Nevertheless, some drawbacks of PLGA nanoparticles including rapid opsonization by cells of mononuclear phagocytic system (MPS), premature drug release, severe inter-particle aggregation under physiological condition and lack of tumor acidity-responsive drug liberation profoundly limited their clinical translation [16,19,20].

Chitosan, a cationic polysaccharide generated from deacetylation of natural chitin, has been often used to modify the PLGA nanoparticles due to its biocompatibility, biodegradability, mucoadhesive and pH-responsive properties [19–25]. Although the in vivo biodegradability mechanism of chitosan has not been clearly understood, some studies pointed out the degradation of chitosan and its micro/nanoparticles by lysozyme, which is available in human body especially in the lungs [26]. It has been demonstrated that chitosan and its derivatives endowed PLGA nanoparticles with reduced premature drug leakage, pH-dependent drug release performance and enhanced cellular uptake [20,23–25]. As reported by Lu et al. [24], the chitosan-coated PLGA nanoparticles serving as paclitaxel (PTX) vehicles not only appreciably declined the initial burst liberation of PTX but also accelerated drug release with pH decrease from 7.4 to 5.0. Compared to free PTX, the PTX-loaded chitosan-modified PLGA nanoparticles were internalized by MDA-MB-231 cells in more efficient manner due to their positively-charged surfaces, thereby displaying higher cytotoxicity. Furthermore, Bhattarai's group developed the chitosan-modified PLGA nanoparticles to deliver diclofenac sodium (DS) [25], a nonsteroidal anti-inflammatory drug. They found that the coating of chitosan on the surfaces of DS-encapsulated PLGA nanoparticles remarkably accelerated DS release from nanoparticles in acidic aqueous solutions owing to the promoted protonation and water-solubility of chitosan. As described above, some disadvantages of PLGA nanoparticles could be conquered by chitosan surface coating, however, the positively-charged nanoparticles were apt to adsorb opsonins and negatively-charged serum proteins during blood circulation to cause their rapid body elimination and tissue toxicity, thus being not beneficial to accumulate within tumors [27–29]. Therefore, the decoration of PLGA nanoparticles with chitosan alone still faced great challenges in tumor-targeted drug delivery.

To the best of our knowledge, it has been recently demonstrated that the surface coating of PLGA nanoparticles with both chitosan and hydrophilic poly(ethylene glycol) (PEG) can significantly prolong their blood circulation time by inhibiting the phagocytic effects [19,29,30]. For example, Sahoo and co-workers found that, through the blending of chitosan and PEG segments with PTX-encapsulated PLGA nanoparticles, the obtained dual chitosan/PEG-coated PLGA nanoparticles loaded with PTX showed remarkably prolonged blood circulation time and reduced macrophage uptake [19]. Also, the PEG and chitosan coating of PTX-encapsulated PLGA nanoparticles considerably promoted their cellular uptake and cytotoxicity in various cancer cell lines. In a similar strategy, Liu's group designed the PLGA-based nanoparticles coated with both chitosan oligosaccharide and PEG-poly(D,L-lactic acid) (PDLLA) for tumor targeted delivery of PTX [29]. With the synergistic effect of chitosan oligosaccharide and PEG-PDLLA, the PTX-loaded hybrid nanoparticles not only potently retarded macrophage uptake to prolong the blood circulation time, but also enhanced the selective accumulation and interstitial penetration capacity in tumor region, thus showing outstanding antitumor efficacy against MDA-MB-231 tumor in vivo. Besides, in order to improve liver cancer treatment, the PEG/lactobionic acid (LA)-modified chitosan was covered on the surfaces of PLGA nanoparticles for encapsulation and targeted release of arsenic trioxide (As_2O_3) [30]. Despite of the progress in tumor-targeted drug delivery and antitumor effect of these PLGA nanoparticles equipped with dual surface coating of chitosan and PEG, the approaches of producing these hybrid nanoparticles frequently involved the use of non-biodegradable surfactants (stabilizers) such as poly(vinyl alcohol) and poloxamer, complicated materials, massive organic solvents or multi-step procedures such as double emulsion method, being not favorable to large-scale manufacture and clinical application.

In order to overcome the aforementioned hurdles, in this work, a surfactant-free and one-step nanoprecipitation method was adopted to develop the pH-responsive PEGylated chitosan-decorated PLGA nanoparticles for efficient intracellular delivery of hydrophobic DOX (Figure Scheme 1). To the best of our knowledge, the study regarding the functionalized decoration of PLGA nanoparticles with PEGylated chitosan by a single-step procedure has never been reported. The amphiphilic PEGylated chitosan$_{20k}$ was synthesized by conjugation of chitosan$_{20k}$ (MW 20 KDa) with methoxy PEG carboxylic acid and used as stabilizer. Through the co-assembly of amphiphilic PEGylated chitosan$_{20k}$ adducts, hydrophobic PLGA segments and DOX molecules in aqueous solutions at pH 8.5, the DOX-encapsulated hybrid PEGylated chitosan$_{20k}$/PLGA nanoparticles were fabricated and characterized by variable angle dynamic/static light scattering (DLS/SLS), transmission electron microscopy (TEM) and zeta potential measurements. Also, the effects of chain length of chitosan from PEGylated chitosan adducts on the colloidal structure of the hybrid nanoparticles and their colloidal stability in serum-containing aqueous solutions as well as acidity-responsive structural transformation were investigated. In addition to the in vitro DOX release performance, the in vitro cellular uptake of DOX-loaded hybrid nanoparticles by prostate TRAMP-C1 cancer cells and macrophage-like RAW264.7 cells and their cytotoxicity were explored. To evaluate the antitumor efficacy of DOX-carrying hybrid nanoparticles, the studies of in vivo tumor growth were further conduced in this work.

2. Experimental section

2.1. Materials

DOX (in the hydrochloride salt form) was purchased from Carbosynth Ltd. (UK). PLGA (50/50) (Inherent viscosity: 0.15 dL/g) was acquired from Green Square (Taiwan). Chitosan$_{5k}$ oligosaccharide (MW 5.0 kDa, 81% degree of deacetylation) and chitosan$_{20k}$ (MW 20.0 kDa, 90% degree of deacetylation) were obtained from Glentham Life Science Ltd. (UK). Methoxy poly(ethylene glycol) (mPEG) (MW 5.0 kDa), 3-(4,5-Dimethylthiazol-2-yl)-2,5-diphenyltetrazolium bromide (MTT), dulbecco's modified Eagle medium (DMEM), RPMI-1640 medium, D_2O (99.9 atom % D), and $CDCl_3$ (99.8 atom % D) were purchased from Sigma-Aldrich (USA). N-(3-Dimethylaminopropyl)-N′-ethyl-carbodiimide hydrochloride (EDC, 95%) was attained from Matrix Scientific (USA). Pyrene (98%), N-hydroxysuccinimide (NHS, 98%) and succinic anhydride (99%) were acquired from Alfa Aesar (USA). Fetal bovine serum (FBS) was purchased from Hyclone (USA). Hoechst 33342 was purchased from Invitrogen. Deionized water was produced from Milli-Q Synthesis (18 MΩ, Millipore). All other chemicals were reagent grade and used as received. TRAMP-C1 cells (murine prostate cancer cell line), CT-26 cells (murine colon adenocarcinoma cell line) and RAW264.7 cells were acquired from Food Industry Research and Development Institute (Hsinchu City, Taiwan).

2.2. Synthesis and characterization of PEGylated chitosan adducts

Through the ring-opening reaction of succinic anhydride with mPEG, the mPEG-COOH utilized in the work was prepared as described in our previous work [31]. The PEGylated chitosan$_{20k}$ was synthesized by the EDC/NHS-mediated amindation of chitosan$_{20k}$ and mPEG-COOH (Scheme 2). Briefly, chitosan$_{20k}$ (300 mg) was dissolved in 1.0 vol% acetic acid aqueous solution. The mPEG-COOH (720 mg), NHS (331 mg) and EDC (552 mg) were dissolved in deionized water (12 mL). Next, the

chitosan-containing solution was added dropwise into the above solution under stirring. The solution was stirred at 25 °C for 48 h, followed by dialysis (Cellu Sep MWCO 6000–8000) against deionized water to eliminate NHS and EDC. The product was collected by lyophilization. For comparison, the PEGylated chitosan$_{5k}$ was prepared by the same way. The chemical structure of PEGylated chitosan was characterized by Fourier transform infrared (FT-IR) spectroscopy (FT-720, HORIBA, Japan) using KBr pellet for the sample preparation, and proton nuclear magnetic resonance (^{1}H NMR) spectroscopy (Agilent DD2 600 MHz NMR spectrometer) using D_2O as the solvent. Because the fluorescence intensity ratios (I_3/I_1) of the third vibrionic band at 381.5 nm to the first at 371.5 nm of the fluorescence emission spectra of pyrene are sensitive to the hydrophobic microenvironment of the polymeric assemblies [31–33], the hydrophobic property of PEGylated chitosan in aqueous solutions of various pH was studied by fluorescence measurement using pyrene as a fluorescence probe. Aliquots (20.0 μL) of pyrene in acetone (3.0×10^{-5} M) was evaporated in vials, and the aqueous solutions of PEGylated chitosan at the prescribed pH (1.0 mL) were added to obtain the PEGylated chitosan solutions with a constant pyrene concentration of ca 6.0×10^{-7} M. The fluorescence emission spectra of pyrene in the PEGylated chitosan solutions were attained with a Hitachi F-2700 fluorescence spectrometer. The excitation of 336 nm was adopted and the emission wavelength ranging from 350 to 500 nm was recorded. The fluorescence intensity ratios (I_3/I_1) of pyrene in the PEGylated chitosan solutions were determined.

2.3. Preparation of PEGylated chitosan/PLGA nanoparticles (PCPNs)

The PC$_{20k}$PNs (0.38) ([PEGylated chitosan$_{20k}$]/[PLGA] = 0.38/1 (*w*/w)) were prepared by single-step nanoprecipitation method. Briefly, PEGylated chitosan$_{20k}$ (1.5 mg) and PLGA (4.0 mg) were completely dissolved in DMSO (0.4 mL), followed by dropwise addition into pH 8.5 phosphate buffer (ionic strength 0.01 M, 1.6 mL) under stirring. The solution was gently stirred at room temperature for 1 h and then dialyzed (Cellu Sep MWCO 12000–14,000) with pH 8.5 phosphate buffer at 4 °C to attain the PC$_{20k}$PNs. After freeze-drying, the yield of PC$_{20k}$PNs was determined to be 96.8%. For comparison, the PC$_{5k}$PNs composed of PEGylated chitosan$_{5k}$ and PLGA, and PLGA nanoparticles (PNs) without PEGylated chitosan decoration were obtained in a similar manner.

2.4. Preparation of DOX-loaded PCPNs (DOX-PCPNs)

To acquire hydrophobic DOX in free base form, DOX hydrochloride was dissolved in DMSO containing excess triethylamine (3.0-fold excess in molar concentration with respect to DOX) with stirring in dark overnight. The DOX-PC$_{20k}$PNs (0.38) were prepared as follows. PEGylated chitosan$_{20k}$ (1.5 mg), PLGA (4.0 mg) and DOX (0.2 mg) dissolved in DMSO (0.4 mL) were added dropwise into pH 8.5 phosphate buffer (1.6 mL). The solution was stirred at room temperature for 1 h, followed by dialysis (Cellu Sep MWCO 12000–14,000) against pH 8.5 phosphate buffer at 4 °C for 24 h to eliminate unloaded DOX and DMSO. For comparison, DOX-PC$_{20k}$PNs (0.13), DOX-PC$_{5k}$PNs (0.38) and DOX-PNs were fabricated in a similar approach.

2.5. Structural characterization

The mean hydrodynamic diameter (D_h) and particle size distribution of pristine PCPNs, PNs, DOX-PCPNs and DOX-PNs in aqueous solutions were measured by a Brookhaven BI-200SM goniometer equipped with a BI-9000 AT digital correlator using a solid-state laser (35 mW, $\lambda = 637$ nm) detected at a scattering angle of 90°. The zeta potential of the nanoparticles in aqueous solutions was determined by a Litesizer 500 (Anton Paar, USA). The data shown herein were an average of at least triplicate measurements. Moreover, in order to explore the structural characteristics of the PC$_{20k}$PNs, ^{1}H NMR measurement of the freeze-dried PC$_{20k}$PNs dispersed in D_2O was conducted with Agilent DD2 600 MHz NMR spectrometer. To get insight into the morphology of DOX-PC$_{20k}$PNs in aqueous solution at pH 7.4 and 5.5, respectively, in addition to the angular dependence of the autocorrelation functions, the ratio of the root-mean-square radius of gyration (R_g) to the mean hydrodynamic radius (R_h) of DOX-PC$_{20k}$PNs was obtained by angular dependent dynamic and static light scattering (DLS/SLS) measurements using the aforementioned instrument. The R_g of DOX-PC$_{20k}$PNs was quantitatively determined using the Berry plot of the scattering intensity ($I_{ex}^{1/2}$) versus the square of the scattering vector (q^2) from the angle-dependent measurements of the light scattering intensity. On the other hand, TEM images of pristine PC$_{20k}$PNs and DOX-PC$_{20k}$PNs negatively stained with uranyl acetate (2.0 wt%) were gained from a JEOL JEM-1400 CXII microscope. The fluorescence spectra of free DOX, DOX-PC$_{20k}$PNs and pristine PC$_{20k}$PNs in phosphate buffered saline (PBS) were obtained using a Hitachi F-2700 fluorescence spectrometer.

2.6. DOX loading efficiency and content

To quantify DOX encapsulated within nanoparticles, a small portion of the purified aqueous solutions of DOX-carrying nanoparticles was withdrawn and then diluted with DMSO to a volume ratio of DMSO/phosphate buffer = 9/1 for drug extraction. The absorbance of DOX at 480 nm was measured using a UV/Vis spectrophotometer (U2900, Hitachi, Japan). The calibration curve employed for drug loading analysis was established by absorbance of DOX with various concentrations in DMSO/phosphate buffer (9/1 (*v*/v)) solutions. The drug loading efficiency (DLE) and drug loading content (DLC) were obtained by the following equations:

$$\text{DLE}\ (\%) = (\text{weight of loaded DOX}/\text{weight of DOX in feed}) \times 100\%$$

$$\text{DLC}\ (\%) = (\text{weight of loaded DOX}/\text{total weight of the DOX} - \text{loaded nanoparticles}) \times 100\%$$

2.7. In vitro DOX release profiles

To explore in vitro DOX release of DOX-PNs and DOX-PC$_{20k}$PNs, the aqueous solutions (1.0 mL) of the DOX-carrying nanoparticles was dialyzed (Cellu Sep MWCO 12000–14,000) with PBS (pH 7.4, 20 mL) and acetate buffer (pH 5.5, 20 mL) at 37 °C, respectively. At the prescribed time intervals, 0.5 mL of the dialysate was taken for analysis and replaced with an equal volume of fresh buffer. To quantify the amount of DOX release, the DOX fluorescence in the range from 350 to 650 nm was determined by fluorescence measurement using a Hitachi F-2700 fluorescence spectrometer. The concentration of DOX was attained by the appropriate calibration curve of DOX with different concentrations in aqueous solution of either pH 5.5 or 7.4.

2.8. In vitro cellular uptake

The flow cytometer (Guava easyCyte HT, Merk Millipore) was utilized to assess cellular uptake of free hydrophobic DOX, DOX-PC$_{20k}$PNs and DOX-PNs (DOX concentration = 2.5 μM) by TRAMP-C1 cells at 37 °C. After 4 h incubation, the treated TRAMP-C1 cells (2×10^5 cells/well) were detached with trypsin-EDTA solution and then dispersed in PBS (0.7 mL), giving a cell suspension containing a minimum of 1×10^4 cells. TRAMP-C1 cells (2×10^5 cells/well) seeded onto 22 mm round glass coverslips in 6-well plates were incubated with free hydrophobic DOX, DOX-PNs and DOX-PC$_{20k}$PNs (0.38) (DOX concentration = 1.25 μM), respectively, at 37 °C for 4 h. After being washed twice with HBSS and immobilized with 4% formaldehyde, cell nuclei were stained with Hoechst 33342. The cellular images were attained using a confocal laser scanning microscope (CLSM) (Olympus, FluoView FV3000, Japan) equipped with a Hoechst set (Ex. 405 nm) and a DOX set (Ex. 488 nm). On the other hand, RAW264.7 cells (2×10^5 cells/well) seeded onto 22 mm round glass coverslips in 6-well plates were incubated with DOX-

PNs and DOX-PC_{20k}PNs (0.38) (DOX concentration = 1.25 μM), respectively, at 37 °C for 30 min and 1 h. The phagocytosis of DOX-PNs and DOX-PC_{20k}PNs (0.38) by RAW264.7 cells was observed by CLSM based on the aforementioned method.

2.9. In vitro cytotoxicity

TRAMP-C1 cells seeded in a 96-well plate at a density of 1×10^4 cells/well in DMEM (100 μL) containing 10% FBS and 1% penicillin were incubated at 37 °C for 24 h. The medium was then replaced with 100 μL of fresh medium containing either free DOX, DOX-PNs or DOX-PC_{20k}PNs (0.38) at various DOX concentrations or pristine PC_{20k}PNs (0.38), and cells were incubated at 37 °C for 24 h. Afterward, 100 μL MTT (0.25 mg/mL) was added into each well and then incubated at 37 °C for 3 h. Subsequently, the culture medium was discarded, followed by addition of DMSO to dissolve the precipitate and the absorbance of the resulting solution at 570 nm was measured using a BioTek 800TS microplate reader. Furthermore, the cytotoxicity of free DOX and different DOX-loaded nanoparticles against CT-26 cells was evaluated by the aforementioned manner. The data shown herein represent an average of at least triplicate measurements.

2.10. In vivo tumor growth inhibition

Male C57BL/6J mice (6–8 weeks old), acquired from National Laboratory Animal Center (Taiwan), were cared in accordance with the Guidance Suggestions for the Care and Use of Laboratory Animals, approved by the Administrative Committee on Animal Research in the Chung Shan Medical University (Taiwan) (IACUC Approval No: 2514). To build tumor model, 8×10^6 TRAMP-C1 cells were subcutaneously injected into the right thigh of mice. Tumor volume (V) was calculated as follows: $V = L \times W^2/2$, where L and W are the tumor dimensions at the longest and the shortest points, respectively. After tumor volume had enlarged to 80–100 mm^3, the mice were randomly divided into 4 groups (3 in each group) and separately intravenous (i.v.) injected with PBS, free DOX, DOX-PNs and DOX-PC_{20k}PNs (0.38) at a DOX dosage of 0.51 mg/kg. Each group was treated with a total of two doses at days 0 and 3. Tumor volume and body weight of mice were measured every 2 days. Tumor growth in the various treatment modalities was monitored until 14 days post-injection. The tumor volumes of various groups were normalized against the original volumes to evaluate the antitumor efficacy. The tumors were then isolated from the euthanized mice and weighted. The ratio of tumor weight to body weight (tumor/body weight) employed as a quantitative measure of therapeutic efficacy was calculated by the following formulas.

$$\text{Tumor} \Big/ \text{body weight} = \frac{W_{tumor}}{W_{body.}}$$

W_{tumor} and W_{body} represent the weight of tumor and mice after the experiment, respectively.

After the end of treatment, all the tumor-bearing mice were sacrificed by CO_2 euthanasia. The mice tissues, including heart, liver, spleen, lung, kidney and xenograft tumor, were excised, fixed with 10% formalin and then embedded with paraffin wax. The embedded tissues were sectioned in to 5 μm for performing hematoxylin and eosin (H&E) staining, Ki67 immunohistochemical staining and apoptotic cells staining. For apoptosis detection, the TUNEL detection kit (Roche, Penzberg, Germany) was adopted. The automated TissueFAXS PLUS system was used to acquire section images (TISSUE GNOSTICS, Vienna, Austria).

2.11. Statistical analysis

All data are reported as the mean ± standard deviation (SD). Data analyses for two groups were carried out using Student's *t*-test. Statistical significance is indicated as (n.s.) $P > 0.05$, (*) $P < 0.05$ and (**) $P < 0.01$.

3. Results and discussion

3.1. Synthesis and characterization of PEGylated chitosan

Based on our previous work [31], through the ring-open reaction of succinic anhydride with the hydroxyl end of mPEG segments, the mPEG-COOH employed in this study was attained and characterized by FT-IR and ^{1}H NMR spectroscopy (Figs. S1 and S2). After the grafting reaction of mPEG-COOH with $chitosan_{20k}$ by EDC/NHS-mediated amidation, the PEGylated $chitosan_{20k}$ was obtained. For comparison, the PEGylated $chitosan_{5k}$ was also synthesized. The characteristic bands of mPEG and $chitosan_{20k}$ segments were observed in FT-IR spectrum of PEGylated $chitosan_{20k}$ (Fig. S1). Also, the ^{1}H NMR spectrum of PEGylated $chitosan_{20k}$ (Fig. 1a) showed the appearance of the feature proton signals of mPEG-COOH at δ 3.7 and 3.4 ppm, respectively, and of chitosan at δ 3.5–4.0 and 2.0 ppm, respectively. These results demonstrate the successful PEGylation of $chitosan_{20k}$. Based on the signal integral ratio of the methoxy protons of mPEG-COOH at δ 3.4 ppm and the *N*-acetyl protons of chitosan at δ 2.1 ppm, the degree of substitution of chitosan with mPEG-COOH defined as the number of mPEG segments per 100 glucosamine units was estimated to be ca. 12.9. In view of the water-insoluble nature of pH-responsive $chitosan_{20k}$ (pKa 6.5) in basic aqueous solution and the hydrophilic property of mPEG segments, it was assumed that the resulting PEGylated $chitosan_{20k}$ could exhibit an amphiphilic character in response to external pH change. Notably, as shown in Fig. 2a, the I_3/I_1 value of pyrene in aqueous solutions of PEGylated $chitosan_{20k}$ was appreciably increased from 0.66 to 0.75 with solution pH being adjusted from 5.5 to 8.5. Also, in addition to the formation of colloidal particles (ca. 200 nm in D_h) in the PEGylated $chitosan_{20k}$ solution at pH 8.5 attained by DLS characterization (Fig. S3), a significant conversion in zeta potential of PEGylated $chitosan_{20k}$ from +20 to 0 mV with the same pH stimulation was observed (Fig. 2b). The findings evidently proved our postulation that the PEGylated $chitosan_{20k}$ adducts turned from hydrophilic to amphiphilic property upon the pH rise owing to the increased hydrophobicity of non-protonated $chitosan_{20k}$ segments, thus being prone to self-assemble into polymeric assemblies with hydrophobic $chitosan_{20k}$-rich microdomains, where the nonpolar pyrene resides. In contrast, the PEGylated $chitosan_{20k}$ chains at pH 5.5 were highly hydrated state due to the considerable protonation of $chitosan_{20k}$ segments. Distinct from the PEGylated $chitosan_{20k}$ adducts possessing amphiphilic feature at pH 8.5, the PEGylated $chitosan_{5k}$ chains undergoing appreciable deprotonation of $chitosan_{5k}$ segments in response to pH increase from 5.5 to 8.5 still retained quite hydrated as reflected by their reduced zeta potential and the unvaried I_3/I_1 value (ca. 0.66) of pyrene in their solution (Fig. 2a and b). This signifies that, compared to the PEGylated $chitosan_{5k}$, the PEGylated $chitosan_{20k}$ with relatively longer chitosan segments in basic aqueous solution (pH 8.5) are apt to associate into polymeric assemblies upon strong hydrophobic attraction driven by zipper-like hydrogen bonds between non-protonated $chitosan_{20k}$ segments. A similar result that the water solubility of chitosan segments was remarkably decreased by the increased molecular weight of chitosan was also reported by You's group [34].

3.2. Preparation and characterization of hybrid PEGylated chitosan/PLGA nanoparticles

Different from some chitosan/PEG-decorated PLGA nanoparticles attained by the multiple-step procedures involving use of surfactants [19,30], in this study, taking advantage of the increased hydrophobicity of amphiphilic PEGylated $chitosan_{20k}$ in basic aqueous phase as described above, the PC_{20k}PNs were fabricated by the surfactant-free one-step co-assembly of PEGylated $chitosan_{20k}$ and hydrophobic PLGA segments ([PEGylated chitosan]/[PLGA] = 0.38/1 (*w*/w)) in aqueous solution of pH 8.5. For comparison, at the same weight ratio of

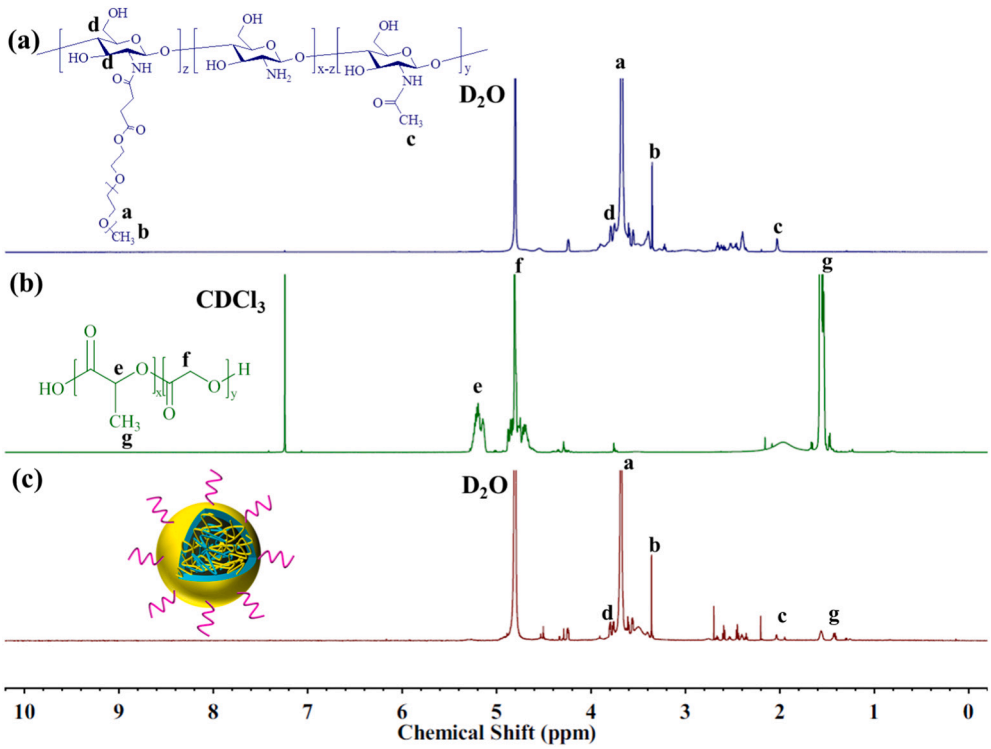

Fig. 1. ^{1}H NMR spectra of (a) PEGylated chitosan$_{20k}$, (b) PLGA, and (c) PC$_{20k}$PNs.

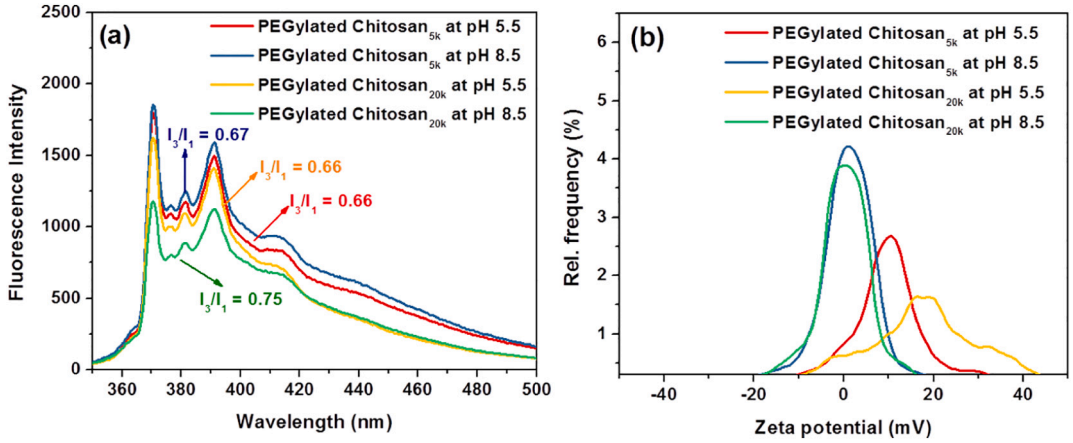

Fig. 2. (a) Fluorescence spectra of pyrene in aqueous solutions of PEGylated chitosan at pH 5.5 and 8.5. (b) Zeta potential profiles of PEGylated chitosan in aqueous solutions at pH 8.5 and 5.5.

PEGylated chitosan and PLGA, the PC$_{5k}$PNs (0.38) were also prepared in a similar manner. As presented in Fig. 3a and Table 1, the PC$_{20k}$PNs (0.38) and PC$_{5k}$PNs (0.38) exhibited a mono-modal size distribution in pH 7.4 PBS and mean D_h of ca. 167.0 and 120.2 nm, respectively, being appreciably larger than that (ca. 57.3 nm) of PNs without PEGylated chitosan decoration. The enlarged particle size of PEGylated chitosan-decorated PLGA nanoparticles could be ascribed to the presence of the additional coating layer and formation of hybrid chitosan/PLGA core structure. Moreover, the zeta potential values of PC$_{20k}$PNs (0.38) and PC$_{5k}$PNs (0.38) in aqueous solution of pH 7.4 determined to be ca. −3.3 and −4.9 mV were prominently lower in comparison with that (ca. −32.8 mV) of PNs (Fig. 3b). Such a significantly declined zeta potential for PEGylated chitosan-decorated PLGA nanoparticles was presumed to that the outer PEGylated chitosan layer could largely shield the negative charges from carboxylic acid end groups on the surfaces of PLGA-rich core. To get insight into the structural characteristic of PC$_{20k}$PNs (0.38) in aqueous solution, the ^{1}H NMR measurement was performed. As shown in Fig. 1, compared with the fully detectable feature proton signals of PLGA in $CDCl_3$ and PEGylated chitosan$_{20k}$ in D_2O, the considerably lowered signal intensity of the methyl protons of PLGA at δ 1.4 ppm and the *N*-acetyl protons of PEGylated chitosan$_{20k}$ at δ 2.1 ppm was observed in the ^{1}H NMR spectrum of PC$_{20k}$PNs (0.38) dispersed in D_2O. Moreover, the feature proton signals at δ 3.7 and 3.4 ppm of mPEG segments from PC$_{20k}$PNs (0.38) maintained obviously detectable. The findings suggest that the chitosan$_{20k}$ chains from PEGylated chitosan$_{20k}$ and PLGA segments are involved mostly in the formation of hybrid hydrophobic core of PC$_{20k}$PNs during co-association at pH 8.5, thereby leading to the corresponding protons undetectable by ^{1}H NMR, while the hydrophilic mPEG segments of PEGylated chitosan$_{20k}$ prefer to dwell at the surfaces of PC$_{20k}$PNs to preserve the segmental flexibility. Based on the above results, it can be concluded that the resulting PC$_{20k}$PNs exhibit a chitosan$_{20k}$/PLGA-constituted hybrid hydrophobic core

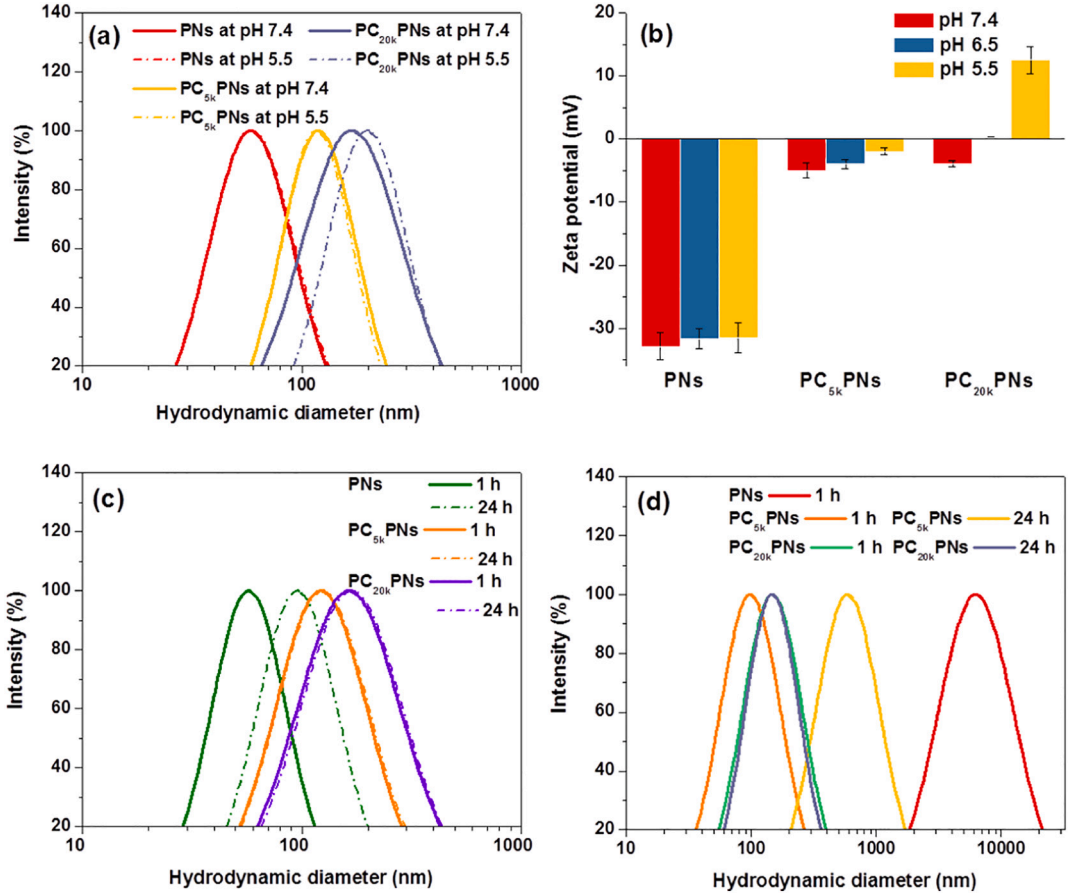

Fig. 3. (a) DLS particle size distribution profiles of PNs, PC_{5K}PNs, PC_{20k}PNs dispersed in aqueous solution of pH 7.4 and 5.5 at 37 °C for 3 h. (b) Zeta potential of PNs, PC_{5k}PNs and PC_{20k}PNs in aqueous solutions. (c) DLS size distribution profiles of PNs and PC_{20k}PNs suspended in pH 7.4 PBS at different time intervals. (d) DLS size distribution profiles of PNs, PC_{5k}PNs and PC_{20k}PNs suspended in PBS containing 10% FBS at different time intervals (1 and 24 h).

Table 1
DLS data and drug loading characteristics of various nanoparticles.

Sample	D_h (nm)	PDI	DLE (%)	DLC (wt%)
PNs	57.3 ± 2.1	0.17 ± 0.02	–	–
PC_{20k}PNs (0.38)	167.0 ± 3.6	0.30 ± 0.02	–	–
PC_{5k}PNs (0.38)	120.2 ± 2.5	0.25 ± 0.01	–	–
DOX-PNs	70.0 ± 2.9	0.18 ± 0.01	79.3 ± 1.5	3.8 ± 0.1
DOX-PC_{20k}PNs (0.38)	148.3 ± 3.8	0.21 ± 0.01	74.8 ± 1.3	2.6 ± 0.1
DOX-PC_{20k}PNs (0.13)	162.0 ± 5.2	0.22 ± 0.04	74.4 ± 3.0	3.2 ± 0.1

stabilized by the outer hydrophilic mPEG segments (Scheme 1).

In view of the pH-responsive property of PEGylated $chitosan_{20k}$, it was expected that the PC_{20k}PNs (0.38) could show the structural transformation in response to pH change. As presented in Fig. 3a, with the solution pH being adjusted from 7.4 to 5.5, the appreciable increase in particle size of PC_{20k}PNs (0.38) from 164 to 193 nm was attained. Also, the zeta potential of PC_{20k}PNs (0.38) was significantly shifted from −3.3 to +14.5 mV in response to pH reduction (Fig. 3b), signifying the extending of the positively-charged $chitosan_{20k}$ segments partially detached from hydrophobic cores toward external aqueous phase. According to these results, such an acidity-triggered enlargement of PC_{20k}PNs (0.38) could be attributed to that the increased protonation of chitosan segments at pH 5.5 facilitates the development of ionic osmotic pressure gradient induced by the positively-charged glucosamine residues located within hybrid chitosan/PLGA core, thereby enhancing water influx into the hybrid nanoparticles to allow nanoparticle swollen (Scheme 1). By contrast, for PNs, their particle size and zeta potential were not obviously changed in the medium pH range 5.0–7.4 due to the lack of acidity-responsive components (Fig. 3a and b). Note that no significant variation in the particle size of PC_{5k}PNs (0.38) in response to pH reduction was attained (Fig. 3a). Due to the weak hydrophobicity of PEGylated $chitosan_{5k}$ at pH 8.5 as revealed in Fig. 2a, it was reasonable to assume that most of $chitosan_{5k}$ segments from PEGylated $chitosan_{5k}$ were only attached on the surfaces of PC_{5k}PNs (0.38) instead of the inner PLGA core (Scheme S1), therefore probably decreasing water inflow and nanoparticle swelling despite of the increased protonation of $chitosan_{5k}$ segments under acidic conditions. Besides, the zeta potential of PC_{5k}PNs only slightly changed (from −4.2 to −2.6 mV) in comparison with that of PC_{20k} PNs under the same pH stimulation (Fig. 3b), being attributed to the substantial shielding of positive charges from short $chitosan_{5k}$ segments by outer mPEG chains.

The particle size of PNs dispersed in 0.15 M PBS at 37 °C was considerably increased from 60 to 140 nm during 24 h while no significant variation in the particle size of PC_{20k}PNs (0.38) and PC_{5k}PNs (0.38) was observed in the same time interval (Fig. 3c). Such an appreciable aggregation of PLGA nanoparticles in aqueous solutions of salt concentration beyond 10 mM was also observed elsewhere [35,36]. Notably, compared to the remarkably enlarged particle size (over 5000 nm) of PNs suspended in 10% FBS-containing PBS within 1 h, the PC_{20k}PNs (0.38) still maintained unchanged particle size (ca. 150.5 nm) within 24 h under the same condition (Fig. 3d). These findings evidently suggest that the PC_{20k}PNs (0.38) exhibit outstanding colloidal stability by steric repulsion property of hydrophilic mPEG shells, while the PNs without hydrophilic surfaces were prone to hydrophobically aggregate into huge particles in aqueous solution, especially in FBS-containing milieu, due to the suppression of the stabilizing electrostatic repulsion in the presence of salt [35,36]. It is noteworthy that, in 10% FBS-

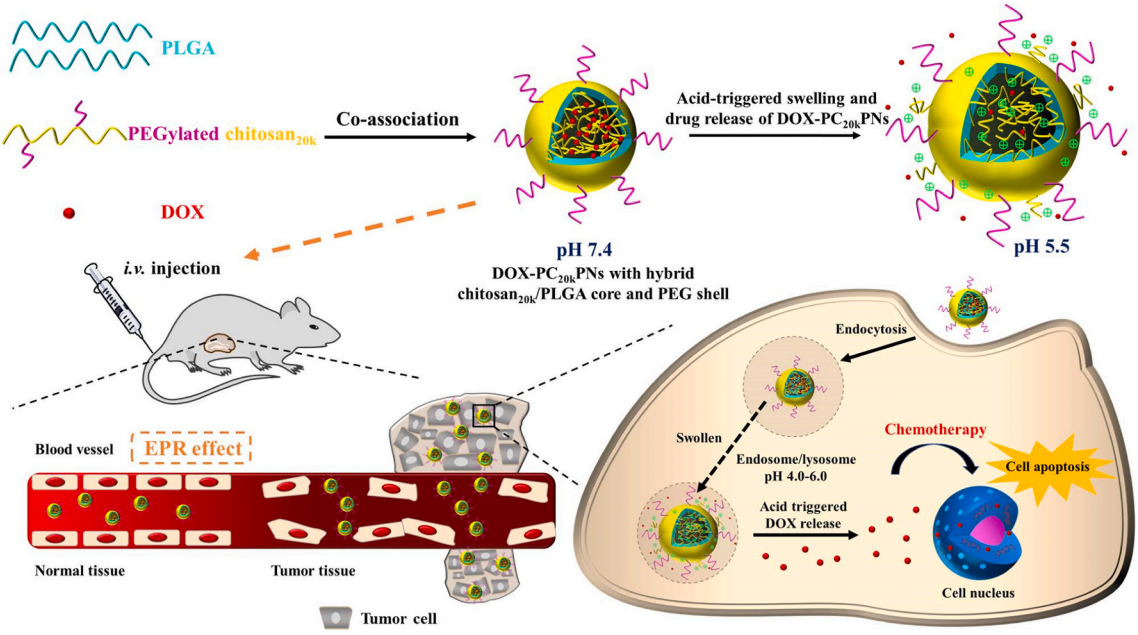

Scheme 1. Illustration of acidity-responsive hybrid PEGylated chitosan$_{20k}$-decorated PLGA nanoparticles as DOX vehicles for effective intracellular drug delivery and cancer treatment.

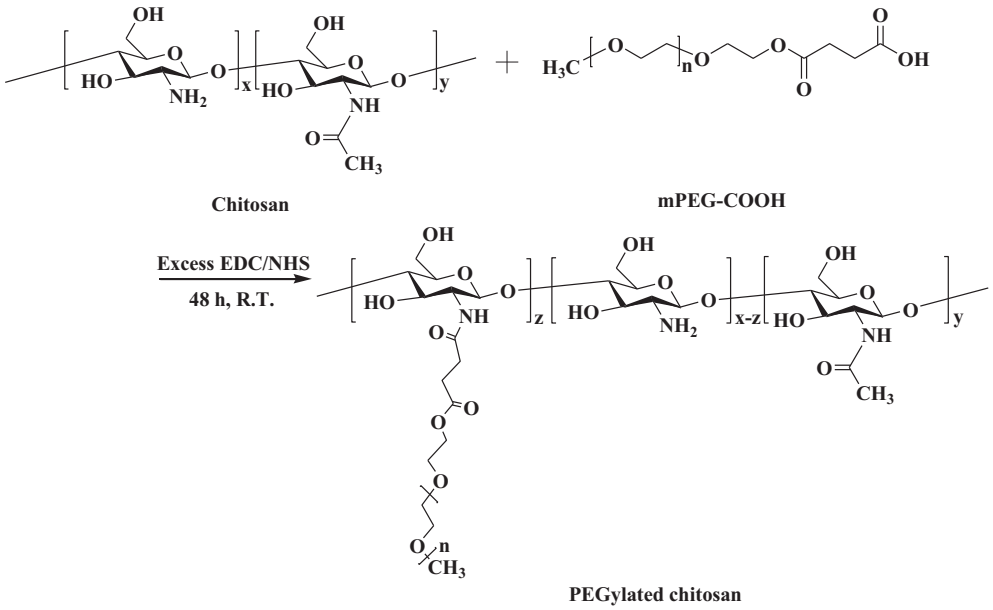

Scheme 2. Synthetic route and chemical structure of PEGylated chitosan adducts.

containing PBS, the PC$_{5k}$PNs (0.38) only showed well dispersion within 1 h, but tended to aggregate into large particles over 24 h as reflected by their increased particle size (Fig. 3d). Compared to PC$_{20k}$PNs (0.38), the PC$_{5k}$PNs had tendency of adsorbing serum proteins in a non-specific manner, thus leading to inter-particle aggregation. Similarly, Zheng et al. reported that the microcapsule surface modified by the PEGylated short chitosan displayed a more remarkable IgG adsorption than the PEGylated long chitosan modified surfaces [37]. For improved tumor-targeted drug delivery, the ideal nanoparticle-based drug delivery carriers should prevent the inter-particle aggregation in serum-containing milieu to prolong their blood circulation time by reducing their uptake by the mononuclear phagocyte system. In this end, based on the superior aqueous colloidal stability and pH-responsive structural transition of PC$_{20k}$PNs, the PC$_{20k}$PNs instead of PC$_{5k}$PNs were utilized as vehicles of hydrophobic DOX in the subsequent study.

3.3. Preparation and characterization of DOX-loaded hybrid nanoparticles

Through one-step co-association of PLGA segments, amphiphilic PEGylated chitosan$_{20k}$ adducts and hydrophobic DOX molecules in aqueous solution of pH 8.5, the DOX-PC$_{20k}$PNs (0.38) were obtained. Note that the DOX-PC$_{20k}$PNs (0.38) at pH 7.4 had appreciably lower DOX fluorescence intensity in comparison with free DOX molecules at the same DOX concentration (Fig. S4). This is attributed to the high local concentration of DOX molecules encapsulated within polymeric

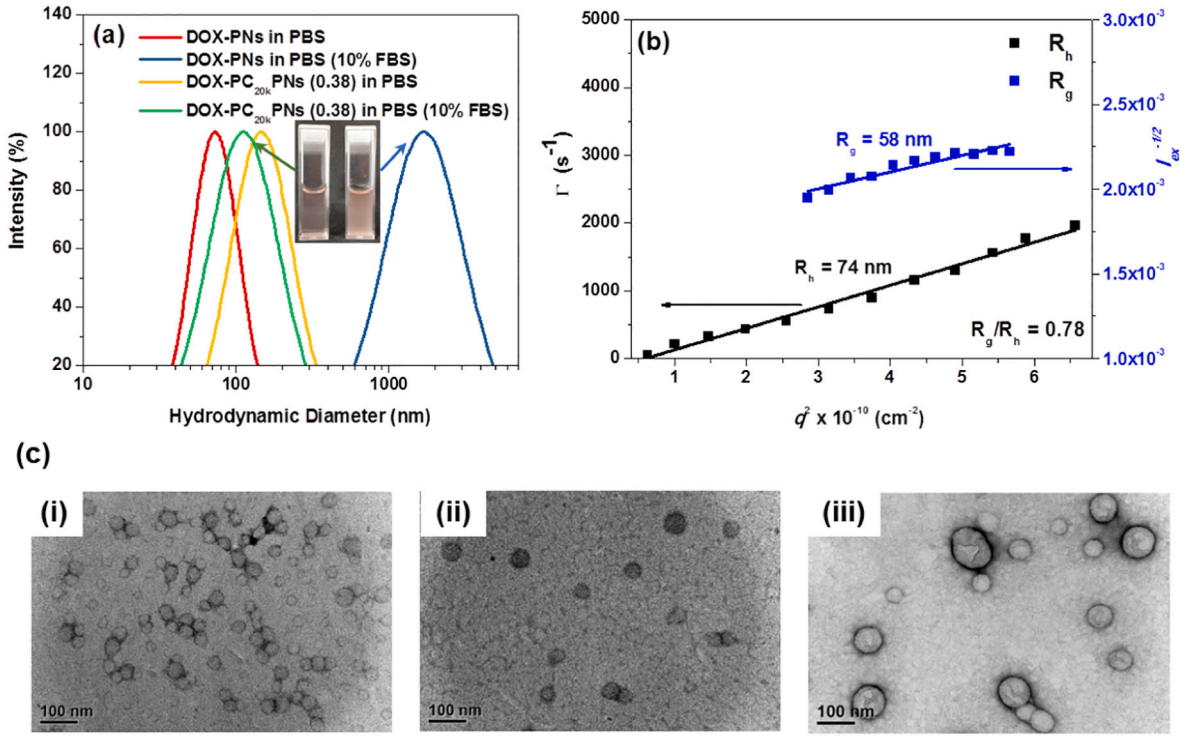

Fig. 4. (a) DLS particle size distribution profiles of DOX-PNs and DOX-PC_{20k}PNs (0.38) dispersed in PBS containing 10% FBS or not at 37 °C for 1 h. (b) Angle-dependent correlation function for R_h and Berry plot for R_g of DOX-PC_{20k}PNs (0.38) in pH 7.4 PBS. (c) TEM images of (i) pristine PC_{20k}PNs (0.38) at pH 7.4 and DOX-PC_{20k}PNs (0.38) at (ii) pH 7.4 and (iii) pH 5.5.

assemblies that unavoidably causes considerable fluorescence quenching of DOX [38,39]. As revealed in Table 1 and Fig. 4a, the DOX-PC_{20k}PNs (0.38) exhibited a nano-scaled particle size (ca. 148.3 nm) and moderate size distribution (PDI 0.21). For DOX-PC_{20k}PNs (0.38), a linear relationship between the relaxation frequency (Γ) and the square of the scattering vector (q^2) was also observed in the angle-dependent DLS examination, clearly illustrating their spherical colloidal form (Fig. 4b). Based on the Berry plot of $I_{ex}^{-1/2}$ versus q^2 from angle-dependent SLS measurement, the R_g value of DOX-PC_{20k}PNs was attained to be ca. 58 nm. In view of the particle form factors innately associated with R_g and R_h, the R_g/R_h ratio is susceptible to assembly topology and thus useful for its structural validation [40,41]. Notably, the gained R_g/R_h ratio (ca. 0.78) of DOX-PC_{20k}PNs (0.38) is essentially comparable to the theoretical value (0.77) of solid sphere-like particles [40,41], signifying their spherical core-shell architecture composed of the DOX-encapsulated hybrid PLGA/chitosan core surrounded by hydrophilic mPEG-rich shells. The TEM images also confirm the spherical shape of DOX-PC_{20k}PNs (0.38) and drug-free PC_{20k}PNs (0.38) (Fig. 4c). Note that the smaller particle size of PC_{20k}PNs (0.38) and DOX-PC_{20k}PNs (0.38) observed by TEM compared to those measured by DLS was attributed to their structural transition from dried (TEM) to swollen (DLS) state [42,43]. Furthermore, different from the remarkably enlarged particle size (ca. 1000 nm) of DOX-PNs in FBS-containing PBS over 1 h due to their rapid hydrophobic aggregation in the absence of hydrophilic surfaces (Fig. 4a), a slightly reduced particle size of DOX-PC_{20k}PNs (0.38) was observed under the same condition, evidently demonstrating that their hydrophilic and flexible mPEG segments could avoid inter-particle aggregation in serum-containing environment. Also, it is worth mentioning that the DOX-PC_{20k}PNs (0.38) dispersed in PBS containing 10% FBS still maintained virtually unvaried particle size within 24 h (Fig. S5). Besides, after being treated with large-volume dilution with PBS, the DOX-PC_{20k}PNs (0.38) retained unchanged particle size (Fig. S6), illustrating their robust colloidal structure. Based on the above data, it was anticipated that the DOX-PC_{20k}PNs (0.38) could preserve structural integrity during blood circulation to prevent inter-particle agglomeration and particle dissolution.

Importantly, when the solution pH was adjusted from 7.4 to 5.5, in addition to the conversion in zeta potential of DOX-PC_{20k}PNs (0.38) from nearly neutral (−1.9 mV) to positive values (+8.1 mV) (Fig. 5a), their particle size was appreciably increased from 148 to 204 nm (Fig. 5b). Such an acidity-induced size enlargement of DOX-PC_{20k}PNs (0.38) was also found in their TEM images (Fig. 4c). It is worthy to notice that the R_g/R_h value of DOX-PC_{20k}PNs (0.38) was increased from 0.78 to 0.88 with pH reduction from 7.4 to 5.5 (Fig. 5c), thereby confirming structural change of the nanoparticles from compact and nondraining to loose and swollen state [44,45]. In agreement with the observed pH-responsive structural transition of drug-free PC_{20k}PNs (0.38) (Fig. 3a and b), the above findings suggest that the enhanced protonation of chitosan segments of DOX-PC_{20k}PNs (0.38) in weak acidic aqueous phase leads to their swelling (Fig. 5d). By contrast, for DOX-PNs, their zeta potential retained virtually invariant with the same pH stimulation owing to the lack of pH-responsive component; however a largely increased particle size was observed, being indicative of their severe aggregation (Fig. 5a and b). Notably, while the DOX-PC_{20k}PNs (0.38) became positively charged on their surfaces in response to the pH reduction to 5.5, the same pH stimulation only rendered the surfaces of DOX-PC_{20k}PNs (0.13) mildly negatively charged (Fig. 5a). Obviously, the surface positive charges of DOX-PC_{20k}PNs under acidic condition were remarkably increased with rising weight ratio of PEGylated $chitosan_{20k}$ and PLGA. As shown in Figs. 3b and 5a, after DOX was encapsulated into PNs, the zeta potential was shifted from −33 to −25 mV. This suggests that DOX molecules could be encapsulated in the hybrid nanoparticles by associating with PLGA segments via hydrophobic interaction as well as electrostatic attraction between their amine moieties and carboxylic end groups from PLGA segments. As presented in Table 1, the DOX-PC_{20k}PNs (0.38) and DOX-PC_{20k}PNs (0.13) showed a satisfied drug loading capacity comparable to DOX-PNs.

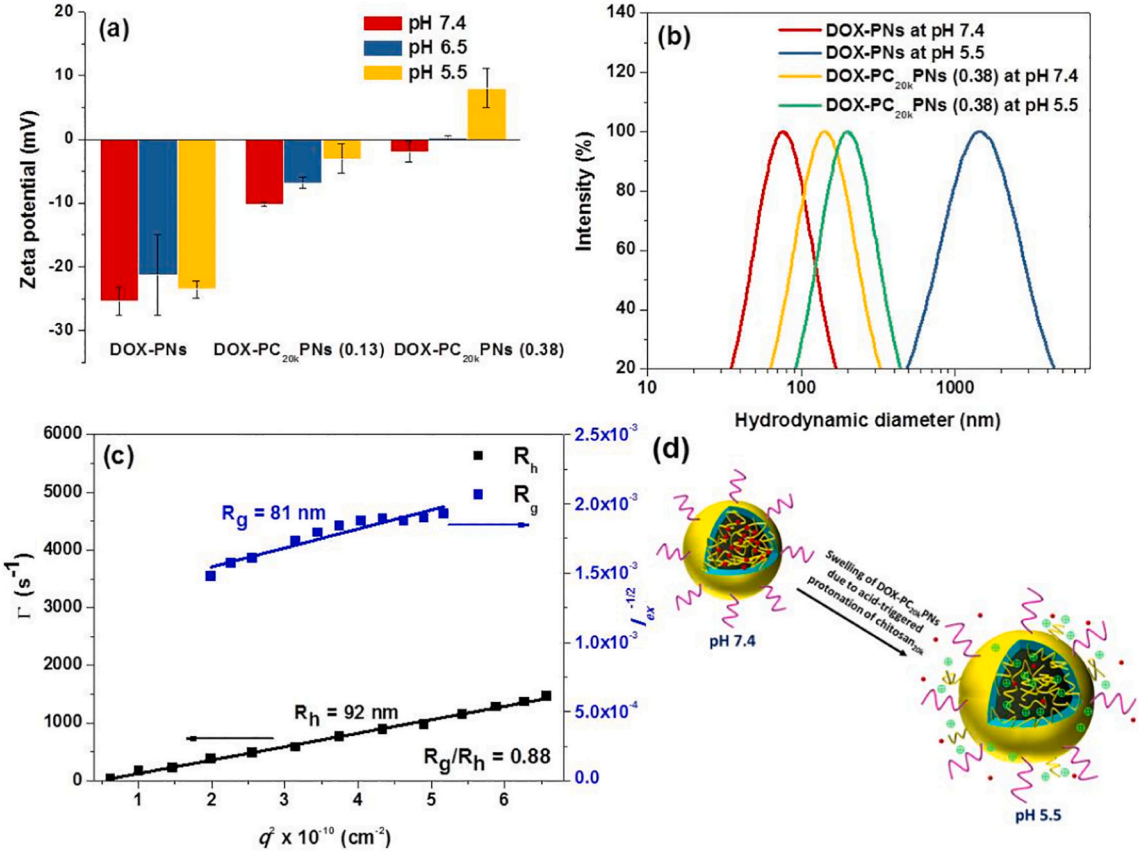

Fig. 5. (a) Zeta potential of DOX-PNs, DOX-PC_{20k}PNs (0.38) and DOX-PC_{20k}PNs (0.13) in aqueous solutions. (b) DLS particle size distribution profiles of DOX-PNs and DOX-PC_{20k}PNs (0.38) dispersed in aqueous solutions of pH 7.4 and 5.5 for 3 h. (c) Angle-dependent correlation function for R_h and Berry plot for R_g of DOX-PC_{20k}PNs (0.38) in pH 5.5 acetate buffer. (d) Schematic illustration of pH-responsive structural transition of DOX-PC_{20k}PNs (0.38).

3.4. *In vitro DOX releases*

For getting insight into the effects of pH-responsive structural transformation of DOX-PC_{20k}PNs (0.38) on drug release, the in vitro DOX release performance at different pH was explored. Considering the weak base property of DOX molecules (pKa 8.6), the release behavior of free DOX molecules in aqueous solutions of different pH values as critical control was explored. In Fig. S7, the rapid outflow of free DOX species (over 80%) across the dialysis tube at pH 7.4 and 5.5 over a period of 6 h was attained, indicating that the slight water solubility difference of free DOX molecules at pH 5.5 and 7.4 did not affect their diffusion behavior. Similar findings have also been reported elsewhere [46,47]. As shown in Fig. 6a, while the cumulative release of DOX from DOX-PC_{20k}PNs was limited to only 30% at pH 7.4 within 2 h, a prominently increased drug release at pH 5.0 was attained (beyond 50%). Over a period of 24 h, the cumulative DOX release performed at pH 5.5 (ca. 85%) was considerably higher than that (ca. 55%) in the milieu of pH 7.4. Similar pH-responsive DOX release behavior was also observed for DOX-PC_{20k}PNs (0.13) (Fig. S8). Such an acidity-triggered rapid DOX release could be ascribed to the following two reasons: First, the increased protonation of chitosan in weak acid environment elicited significant swelling of DOX-PC_{20k}PNs. Second, under acidic condition,

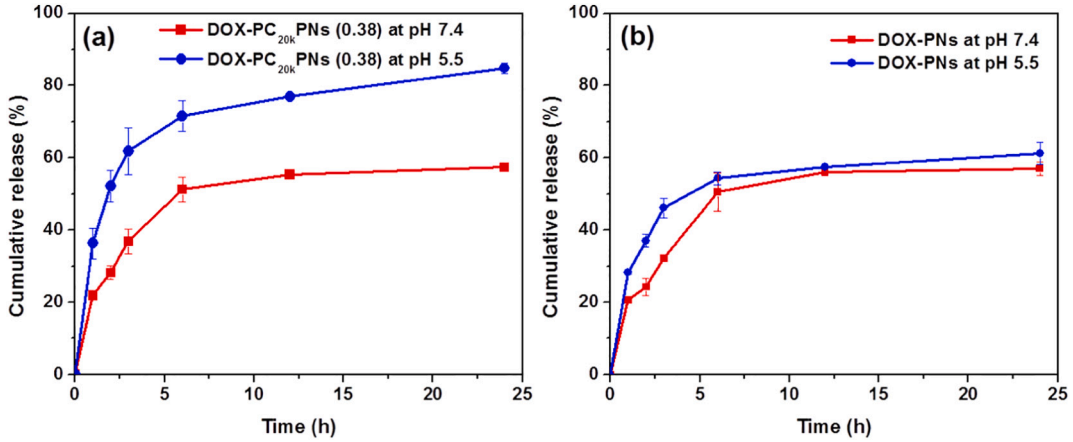

Fig. 6. Cumulative DOX release profiles of (a) DOX-PC_{20k}PNs (0.38) and (b) DOX-PNs in aqueous solutions of pH 7.4 and 5.5 at 37 °C.

the enhanced repulsion force as well as the declined hydrogen bonding among the positively-charged chitosan segments and protonated DOX molecules [48] accelerated DOX outflow from swollen hybrid nanoparticles (Scheme 1). By contrast, for DOX-PNs, similar DOX release profiles at pH 7.4 and 5.5 were observed (Fig. 6b), being attributed to the lack of their pH-dependent structure change. Because the drug release of DOX-PC_{20k}PNs (0.38) was considerably boosted at pH 5.5 compared to that of DOX-PNs, it is anticipated that the DOX-PC_{20k}PNs could realize rapid drug liberation in acidic endosomes and lysosomes of cancer cells, thus facilitating the target of DOX to cell nuclei.

3.5. In vitro cellular uptake

The cellular uptake of DOX-PC_{20k}PNs by TRAMP-C1 cells was evaluated by flow cytometry and CLSM. As shown in the flow cytometric profiles (Fig. 7a), with 4 h incubation, the enhanced DOX fluorescence intensity of TRAMP-C1 cells incubated with either DOX-PC_{20k}PNs (0.38) or DOX-PNs was comparable with that of cells treated with free DOX, indicating the effective cellular uptake of hydrophobic DOX delivered by these nanoparticles. Furthermore, the CLSM images (Fig. 7b) showed that visible DOX fluorescence signals were primarily observed within nucleus and cytoplasm of TRAMP-C1 cells incubated with DOX-PC_{20k}PNs (0.38) at 37 °C for 1 h, whereas no significant DOX fluorescence was obtained from TRAMP-C1 cells incubated with the counterparts at 4 °C for 1 h. The preliminary findings illustrate that the DOX-PC_{20k}PNs (0.38) could be internalized by TRAMP-C1 cells via the energy-consuming endocytosis pathway. Similar results regarding that the cellular uptake of the nanoparticles relied mainly on the energy-dependent endocytosis rather than the passive diffusion were also attained elsewhere [49,50]. As presented in the CLSM images (Fig. 7c), a prominent DOX fluorescence was found in the nucleus area of TRAMP-C1 cells incubated with DOX-PC_{20k}PNs (0.38) at 37 °C for 4 h, being comparable to that of cells treated with free hydrophobic DOX. In agreement with the in vitro release study, DOX molecules were quickly liberated from endocytosed DOX-PC_{20k}PNs (0.38) within acidic endosomes and lysosomes most probably because of remarkable acid-

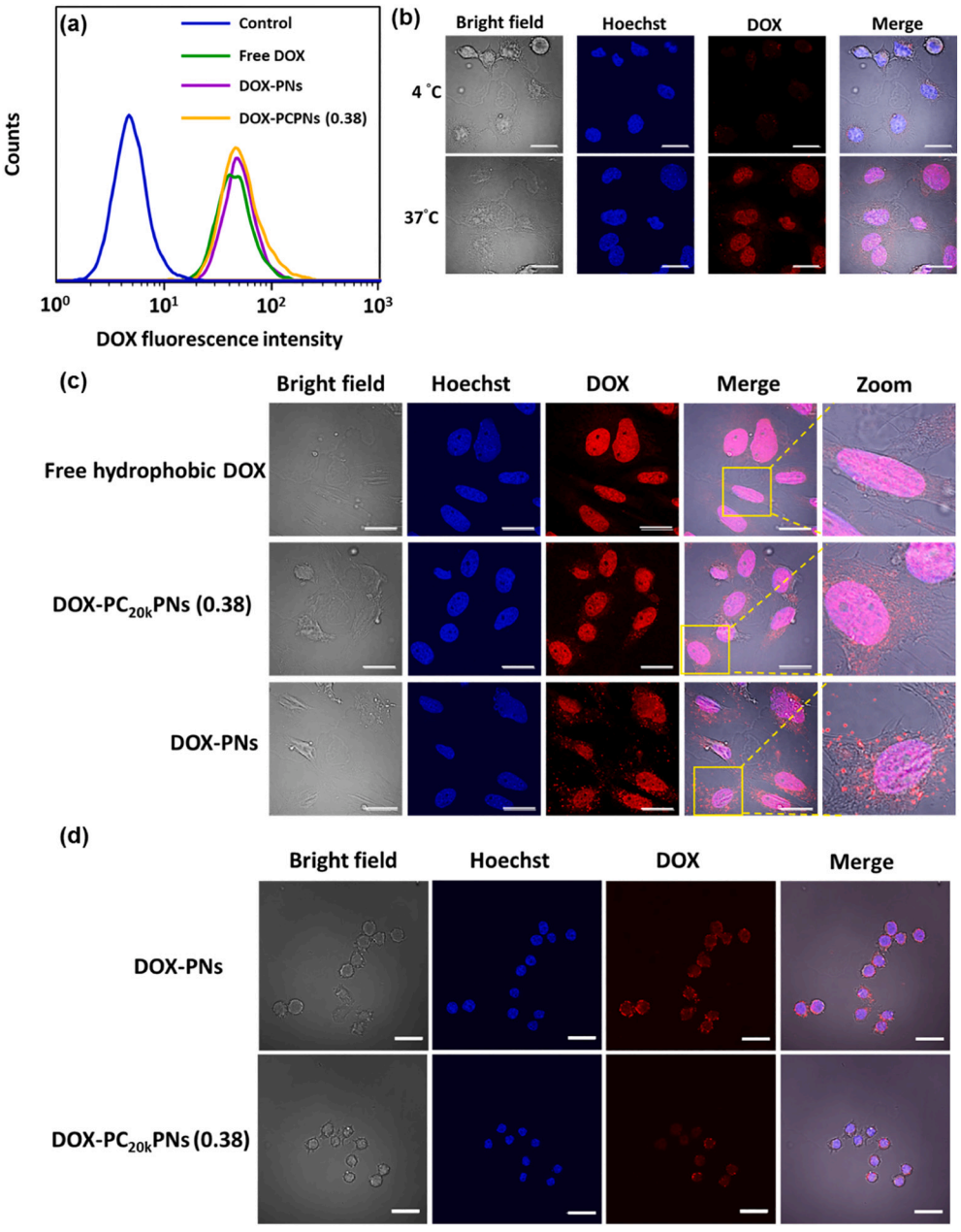

Fig. 7. (a) Flow cytometric histogram profiles of TRAMP-C1 cells incubated with free hydrophobic DOX, DOX-PNs and DOX-PC_{20k}PNs (0.38), respectively, at 37 °C for 4 h (DOX concentration = 2.5 μM). (b) CLSM images of TRAMP-C1 cells incubated with DOX-PC_{20k}PNs (0.38) at 4 and 37 °C, respectively, for 1 h (DOX concentration = 1.25 μM). (c) CLSM images of TRAMP-C1 cells treated with free hydrophobic DOX, DOX-PNs and DOX-PC_{20k}PNs (0.38), respectively, at 37 °C for 4 h (DOX concentration = 1.25 μM). Cell nuclei were stained with Hoechst 33342. Scale bars are 20 μm. (d) CLSM images of RAW264.7 cells incubated with DOX-PNs and DOX-PC_{20k}PNs (0.38), respectively, at 37 °C for 1 h (DOX concentration = 1.25 μM). Cell nuclei were stained with Hoechst 33342. Scale bars are 20 μm.

triggered nanoparticle swelling, thus leading to deposition in a large measure in the cell nucleus (Scheme 1). A similar finding regarding the promoted delivery of hydrophobic DOX toward cell nucleus by smart nanovehicles composed of pH-responsive supramolecular peptide-amphiphiles was also reported by Gu's group [51]. Compared to significant nucleus accumulation of DOX transported by DOX-PC_{20k}PNs (0.38), DOX delivered by DOX-PNs was found remarkably in the cytoplasm and partly in cell nuclei due to the inefficient DOX release from non-pH-responsive DOX-PNs within acidic organelles. On the other hand, to preliminarily explore the anti-MPS clearance capability of DOX-PC_{20k}PNs (0.38), the phagocytosis of the hybrid nanoparticles by RAW264.7 cells was investigated. As shown in Figs. S9 and 7d, RAW264.7 cells incubated with DOX-PC_{20k}PNs for 30 min and 1 h showed considerably lower DOX fluorescence intensity relative to cells treated with DOX-PNs, indicating that the PEG-rich surfaces of DOX-PC_{20k}PNs effectively declined their phagocytosis by monocyte/macrophage-like RAW 264.7 cells. Such a reduced phagocytosis of nanoparticles decorated with PEGylated surfaces by macrophages was also observed elsewhere [29,52]. The above data further illustrate that the DOX-PC_{20k}PNs show great promise in anti-MPS clearance and improved EPR effect.

3.6. In vitro cytotoxicity

The in vitro cytotoxicity of DOX-PC_{20k}PNs (0.38) against TRAMP-C1 cells was assessed by MTT assay. As shown in Fig. 8a, TRAMP-C1 cells incubated with drug-free PC_{20k}PNs (0.38) in the concentration range 27–427 μg/mL for 24 h maintained high viability (over 85%), suggesting that the pristine PC_{20k}PNs (0.38) composed of biocompatible PLGA segments and PEGylated $chitosan_{20k}$ adducts were virtually harmless to TRAMP-C1 cells. Notably, the viability of TRAMP-C1 cells treated with free DOX molecules, DOX-PNs and DOX-PC_{20k}PNs (0.38), respectively, was significantly decreased with increased DOX concentration (Fig. 8b), signifying the anticancer activity of DOX molecules. Importantly, the drug dose required for 50% cellular growth inhibition (IC_{50}) of DOX-PC_{20k}PNs (0.38) was attained to be ca. 1.28 μM, being considerably lower than that (ca. 3.04 μM) of DOX-PNs. In another cell model, mouse colon CT-26 cancer cells, in addition to few cytotoxicity of drug-free PC_{20k}PNs (0.38) (Fig. 8c), the remarkably lower IC_{50} (ca. 3.23 μM) of DOX-PC_{20k}PNs (0.38) in comparison with that (ca. 10.34 μM) of DOX-PNs was also obtained in Fig. 8d. Such a promoted anticancer potency of DOX-PC_{20k}PNs (0.38) relative to DOX-PNs could be ascribed to the following reasons. First, the acidity-induced rapid DOX release from DOX-PC_{20k}PNs (0.38) within acidic endosomes/lysosomes could boost deposition of DOX inside nuclei, thus augmenting the cytotoxicity. Second, the internalization of DOX-PC_{20k}PNs (0.38) by cancer cells was efficiently promoted in comparison to that of DOX-PNs due to their nearly neutrally surfaces and well-dispersed colloidal structure in serum-containing milieu. In view of these findings, the acidity-sensitive hybrid PC_{20k}PNs developed in this work may serve as a carrier to achieve effective intracellular delivery of hydrophobic DOX for improved cancer chemotherapy.

3.7. In vivo tumor growth inhibition

To assess the in vivo antitumor potency of various DOX-loaded nanoparticle formulations, the tumor size of the TRAMP-C1 tumor-bearing mice was monitored post i.v. injection. The tumor volumes (V)

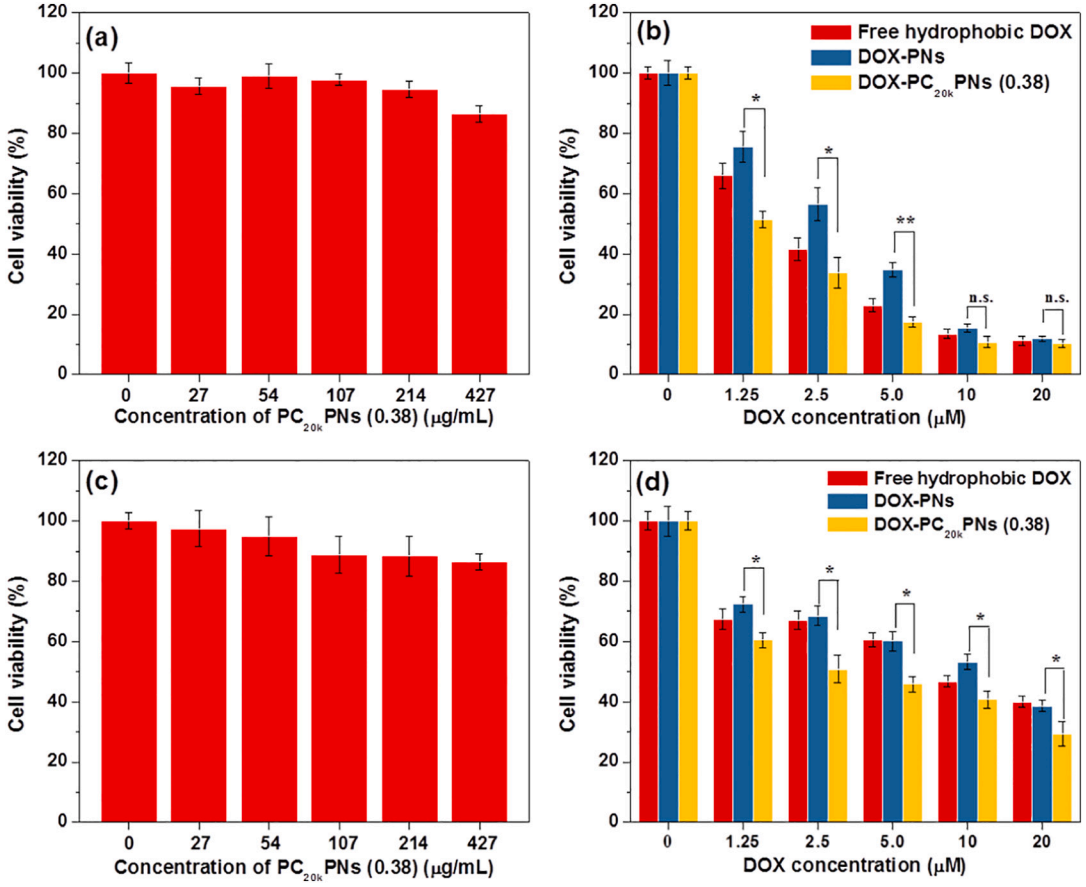

Fig. 8. Cell viability of TRAMP-C1 cells incubated with (a) PC_{20k}PNs (0.38) and (b) free hydrophobic DOX, DOX-PNs and DOX-PC_{20k}PNs (0.38), respectively, at 37 °C for 24 h. Cell viability of CT-26 cells incubated with (c) PC_{20k}PNs (0.38) and (d) free hydrophobic DOX, DOX-PNs and DOX-PC_{20k}PNs (0.38), respectively, at 37 °C for 24 h. $^{*}P < 0.05$, $^{**}P < 0.01$.

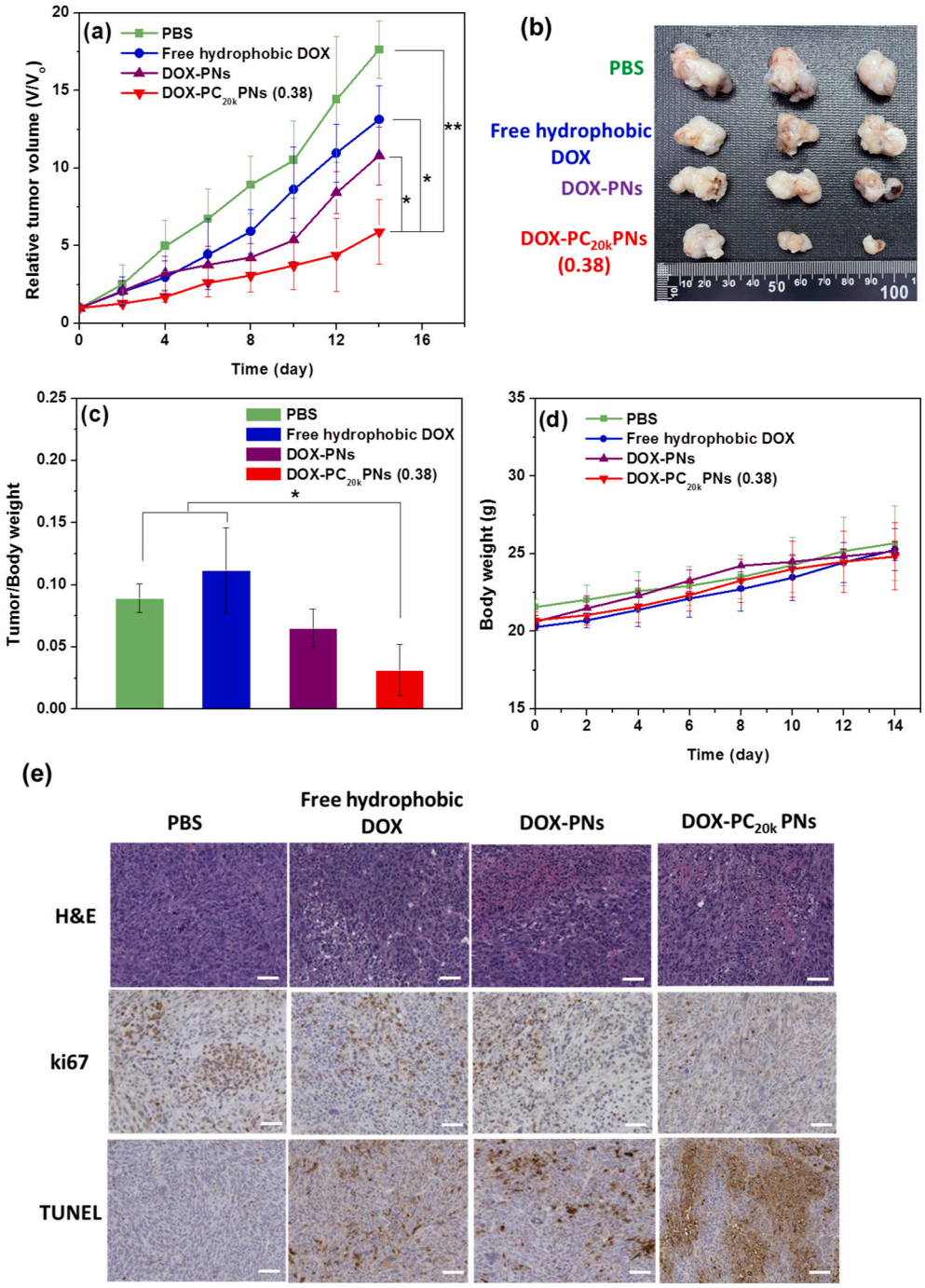

Fig. 9. (a) Tumor growth inhibition profiles of the TRAMP-C1 tumor-bearing mice injected with various formulations (n = 3 per group). (b) Morphology and size of the tumors of each group isolated from the euthanized mice at day 14 after the treatment. (c) Tumor/body weight of mice calculated based on the corresponding data at the end of the study. (d) Body weight of the TRAMP-C1 tumor-bearing mice injected with various formulations (n = 3 per group). (e) Representative images of tumor sections with H&E staining, Ki67 staining and TUNEL assay from tumor-bearing mice receiving different treatments. Scale bars are 50 μm.

were normalized against their original volumes (V_o) to attain the relative tumor volumes (V/V_o). As presented in Fig. 9a, 14 days after treatment, a remarkable 10–14-fold increase in the relative tumor volume of mice treated with free hydrophobic DOX was observed, being only slightly lower than that of the mice treated with PBS. Apparently, the failure of free hydrophobic DOX to hinder tumor growth is mainly resulted from the poor tumor accumulation of DOX. By contrast, during 14 days of treatment, the administration of DOX-loaded nanoparticles led to appreciable inhibition of tumor growth, particularly for DOX-PC_{20k}PNs (0.38). Corresponding to the results of the in vivo tumor growth inhibition, tumors harvested from the euthanized mice treated with DOX-PC_{20k}PNs (0.38) were the smallest among the tumors receiving other treatments (Fig. 9b). Also, the average tumor/body weight ratio (0.025) of DOX-PC_{20k}PNs (0.38) was prominently lower than that (0.063) of DOX-PNs and that (0.11) of free hydrophobic DOX (Fig. 9c). These findings strongly demonstrate that the DOX-PC_{20k}PNs (0.38) exhibited the highest antitumor efficacy by the reduced macrophage uptake to improve EPR effect and effective intracellular DOX delivery (Scheme 1). Furthermore, no considerable variation in the body weights of the treated mice in all groups was obtained (Fig. 9d), signifying that the formulations utilized in this work did not provoke serious acute toxicity.

As revealed in the images of H&*E*-stained tumor sections (Fig. 9e), the tumor sections from the drug-treated mice exhibited appreciable apoptotic regions along with cell shrinkage, nuclear debris and deep karyoplasmic staining, particularly in those from DOX-PC_{20k}PNs (0.38) group, as compared with those from PBS-treated mice. No considerable tissue architecture abnormality was observed in major organs, including

heart, liver, spleen, lung and kidney, of mice from all groups (Fig. S10). A marked decrease in the expression level of Ki67, a proliferation marker, was observed in the tumor sections from DOX-PC_{20k}PNs (0.38) group as compared to other groups, suggesting an anti-proliferative effect of DOX-PC_{20k}PNs (0.38) on xenograft tumors. Notably, apoptotic assay with TUNEL staining further verified that the DOX-PC_{20k}PNs (0.38) elicited high levels of intratumoral cell death. These findings strongly suggest that the DOX-PC_{20k}PNs (0.38) developed herein not only reveal no adverse reaction to normal tissues, but also effectively promote the anti-tumor efficacy. Although further studies on the dose-effect relationship, the indicators of heart, liver, and kidney-related to animal experiments, in vivo DOX distribution and pharmacokinetic as a DOX delivery system are required, the pH-responsive DOX-PC_{20k}PNs (0.38) showed superiority in inhibiting tumor growth by promoting intracellular DOX delivery.

4. Conclusions

In this study, the pH-responsive hybrid nanoparticles from co-assembly of amphiphilic PEGylated $chitosan_{20k}$ and PLGA segments employed as hydrophobic DOX carriers were fabricated by a surfactant-free and one-step nanoprecipitation method. The obtained hybrid nanoparticles were characterized to have a hydrophobic hybrid $chitosan_{20k}$/PLGA core surrounded by hydrophilic mPEG shells. The DOX-PC_{20k}PNs not only maintained outstanding colloidal stability in serum-containing aqueous phase but also accelerated drug liberation in response to pH change from 7.4 to 5.5 upon acid-activated swelling of nanoparticles due to the increased protonation of chitosan segments. Importantly, the results of in vitro cellular uptake and cytotoxicity studies showed that, compared to non-pH-sensitive DOX-PNs, the pH-responsive DOX-PC_{20k}PNs after being endocytosed by TRAMP-C1 cells rapidly released drug, thus facilitating drug deposition in nuclei to augment anticancer potency. Furthermore, the PEG-rich surfaces of DOX-PC_{20k}PNs effectively declined their phagocytosis by monocyte/macrophage-like RAW 264.7 cells. The preliminary in vivo findings showed that the DOX-PC_{20k}PNs not only appreciably suppressed TRAMP-C1 tumor growth compared to free hydrophobic DOX and DOX-PNs, but also revealed no adverse reaction to normal tissues. Overall, the developed pH-responsive DOX-PC_{20k}PNs display great promise to boost cancer chemotherapy.

CRediT authorship contribution statement

Sheng-Jyun Huang: Conceptualization, Methodology, Investigation, Formal analysis,

Tzu-Hao Wang: Investigation, Validation, Resources

Ya-Hsuan Chou: Investigation, Resources

Hui-Min David Wang: Resources

Tsai-Ching Hsu: Resources

Jia-Le Yow: Methodology, Investigation

Bor-Show Tzang: Investigation, Resources, Funding acquisition, Writing-Original Draft

Wen-Hsuan Chiang: Conceptualization, Writing-Original Draft, Writing review& editing, Supervision, Project administration, Funding acquisition.

Acknowledgements

This work is supported by the Ministry of Science and Technology (MOST 108-2221-E-005-024-MY2, MOST 110-2628-E-005-001, MOST110-2731-M-005-001), National Chung Hsing University and Chung Shan Medical University (NCHU-CSMU 11003), Taiwan.

Appendix A. Supplementary data

Supplementary data to this article can be found online at https://doi.org/10.1016/j.ijbiomac.2022.04.209.

References

[1] C. Sun, J. Lu, J. Wang, P. Hao, C. Li, L. Qi, L. Yang, B. He, Z. Zhong, N. Hao, Redox-sensitive polymeric micelles with aggregation-induced emission for bioimaging and delivery of anticancer drugs, J. Nanobiotechnol. 19 (2021) (2021) 14, https://doi.org/10.1186/s12951-020-00761-9.

[2] B. Ma, W. Zhuang, Y. Wang, R. Luo, Y. Wang, pH-sensitive doxorubicin-conjugated prodrug micelles with charge-conversion for cancer therapy, Acta Biomater. 70 (2018) 186–196.

[3] T.A. Debele, K.Y. Lee, N.Y. Hsu, Y.T. Chiang, L.Y. Yu, Y.A. Shen, C.L. Lo, A pH sensitive polymeric micelle for co-delivery of doxorubicin and α-TOS for colon cancer therapy, J. Mater. Chem. B 5 (2017) 5870–5880.

[4] N. Aibani, H. Nesbitt, N. Marino, J. Jurek, C. O'Neill, C. Martin, I.D. Bari, Y. Sheng, K. Logan, S. Hawthorne, A. McHale, J.F. Callan, B. Callan, Electroneutral polymersomes for combined cancer chemotherapy, Acta Biomater. 80 (2018) 327–340.

[5] X. Hu, Y. Zhang, Z. Xie, X. Jing, A. Bellotti, Z. Gu, Stimuli-responsive polymersomes for biomedical applications, Biomacromolecules 18 (2017) 649–673.

[6] P. Wei, G. Gangapurwala, D. Pretzel, M.N. Leiske, L. Wang, S. Hoeppener, S. Schubert, J.C. Brendel, U.S. Schubert, Smart pH-sensitive nanogels for controlled release in an acidic environment, Biomacromolecules 20 (2019) 130–140.

[7] M. Mohammadi, L. Arabi, M. Alibolandi, Doxorubicin-loaded composite nanogels for cancer treatment, J. Control. Release 328 (2020) 171–191.

[8] S. Lv, M. Li, Z. Tang, W. Song, H. Sun, H. Liu, X. Chen, Doxorubicin-loaded amphiphilic polypeptide-based nanoparticles as an efficient drug delivery system for cancer therapy, Acta Biomater. 9 (2013) 9330–9342.

[9] M.E. O'Brien, N. Wigler, M. Inbar, R. Rosso, E. Grischke, A. Santoro, R. Catane, D. G. Kieback, P. Tomczak, S.P. Ackland, F. Orlandi, L. Mellars, L. Alland, C. Tendler, CAELYX breast cancer study group reduced cardiotoxicity and comparable efficacy in a phase III trial of pegylated liposomal doxorubicin HCl (CAELYX/Doxil) versus conventional doxorubicin for first-line treatment of metastatic breast cancer, Ann. Oncol. 15 (2004) 440–449.

[10] L. Lin, X. Liang, Y. Xu, Y. Yang, X. Li, Z. Dai, Doxorubicin and indocyanine green loaded hybrid bicelles for fluorescence imaging guided synergetic chemo/photothermal therapy, Bioconjug. Chem. 28 (2017) 2410–2419.

[11] R. Injac, M. Perse, M. Cerne, N. Potocnik, N. Radic, B. Govedarica, A. Djordjevic, A. Cerar, B. Strukelj, Protective effects of fullerenol C60(OH)24 against doxorubicin-induced cardiotoxicity and hepatotoxicity in rats with colorectal cancer, Biomaterials 30 (2009) 1184–1196.

[12] T. Cheng, J. Liu, J. Ren, F. Huang, H. Ou, Y. Ding, Y. Zhang, R. Ma, Y. An, J. Liu, L. Shi, Green tea catechin-based complex micelles combined with doxorubicin to overcome cardiotoxicity and multidrug resistance, Theranostics 6 (2016) 1277–1292.

[13] S.H. Chen, T.I. Liu, C.L. Chuang, H.H. Chen, W.H. Chiang, H.C. Chiu, Alendronate/folic acid-decorated polymeric nanoparticles for hierarchically targetable chemotherapy against bone metastatic breast cancer, J. Mater. Chem. B 8 (2020) 3789–3800.

[14] M.C. Xiao, Y.H. Chou, Y.N. Hung, S.H. Hu, W.H. Chiang, Hybrid polymeric nanoparticles with high zoledronic acid payload and proton sponge-triggered rapid drug release for anticancer applications, Mater. Sci. Eng. C 116 (2020), 111277.

[15] X. Li, S.A. Valdes, R.F. Alzhrani, S. Hufnagel, S.D. Hursting, Z. Cui, Zoledronic acid-containing nanoparticles with minimum premature release show enhanced activity against extraskeletal tumor, ACS Appl. Mater. Interfaces 11 (2019) 7311–7319.

[16] H. He, E. Markoutsa, Y. Zhan, J. Zhang, P. Xu, Mussel-inspired PLGA/polydopamine core-shell nanoparticle for light induced cancer thermochemotherapy, Acta Biomater. 59 (2017) 181–191.

[17] S. Rezvantalab, N.I. Drude, M.K. Moraveji, N. Güvener, E.K. Koons, Y. Shi, T. Lammers, F. Kiesslin, PLGA-based nanoparticles in cancer treatment, Front. Pharmacol. 9 (2018) 1260.

[18] L. Palanikumar, S. Al-Hosani, M. Kalmouni, V.P. Nguyen, L. Ali, R. Pasricha, F. N. Barrera, M. Magzoub, pH-responsive high stability polymeric nanoparticles for targeted delivery of anticancer therapeutics, Commun. Biol. 3 (2020), https://doi.org/10.1038/s42003-020-0817-4.

[19] S. Parveen, S.K. Sahoo, Long circulating chitosan/PEG blended PLGA nanoparticle for tumor drug delivery, Eur. J. Pharmacol. 670 (2011) 372–383.

[20] F. Chai, L. Sun, X. He, J. Li, Y. Liu, F. Xiong, L. Ge, T.J. Webster, C. Zheng, Doxorubicin-loaded poly (lactic-co-glycolic acid) nanoparticles coated with chitosan/alginate by layer by layer technology for antitumor applications, Int. J. Nanomedicine 12 (2017) 1791–1802.

[21] M. Alibolandi, S.A. Farzad, M. Mohammadi, K. Abnous, S.M. Taghdisi, F. Kalalinia, M. Ramezani, Tetrac-decorated chitosan-coated PLGA nanoparticles as a new platform for targeted delivery of SN38, Artif. Cells Nanomed.Biotechnol. 46 (2018) 1003–1014.

[22] M. Sampath, A. Pichaimani, P. Kumpati, B. Sengottuvelan, The remarkable role of emulsifier and chitosan, dextran and PEG as capping agents in the enhanced

delivery of curcumin by nanoparticles in breast cancer cells, Int. J. Biol. Macromol. 162 (2020) 748–761.
[23] L. Chronopoulou, M. Massimi, M.F. Giardi, C. Cametti, L.C. Devirgiliis, M. Dentini, C. Palocci, Chitosan-coated PLGA nanoparticles: a sustained drug release strategy for cell cultures, Colloids Surf. B 103 (2013) 310–317.
[24] B. Lu, X. Lv, Y. Le, Chitosan-modified PLGA nanoparticles for control-released drug delivery, Polymers 11 (2019) 304.
[25] S. Khanal, U. Adhikari, N.P. Rijal, S.R. Bhattarai, J. Sankar, N. Bhattarai, pH-responsive PLGA nanoparticle for controlled payload delivery of diclofenac sodium, J. Funct. Biomater. 7 (2016) 21.
[26] N. Islam, I. Dmour, M.O. Taha, Degradability of chitosan micro/nanoparticles for pulmonary drug delivery, Heliyon 5 (2019), e01684.
[27] R.R. Arvizo, O.R. Miranda, D.F. Moyano, C.A. Walden, K. Giri, R. Bhattacharya, J. D. Robertson, V.M. Rotello, J.M. Reid, P. Mukherjee, Modulating pharmacokinetics, tumor uptake and biodistribution by engineered nanoparticles, PLoS One 6 (2011), e24374.
[28] F. Alexis, E. Pridgen, L.K. Molnar, O.C. Farokhzad, Factors affecting the clearance and biodistribution of polymeric nanoparticles, Mol. Pharm. 5 (2008) 505–515.
[29] G. Wang, Y. Chen, P. Wang, Y. Wang, H. Hong, Y. Li, J. Qian, Y. Yuan, B. Yu, C. Liu, Preferential tumor accumulation and desirable interstitial penetration of poly (lactic-co-glycolic acid) nanoparticles with dual coating of chitosan oligosaccharide and polyethylene glycol-poly(D, L-lactic acid), Acta Biomater. 29 (2016) 248–260.
[30] X. Song, J. Wang, Y. Xu, H. Shao, J. Gu, Surface-modified PLGA nanoparticles with PEG/LA-chitosan for targeted delivery of arsenic trioxide for liver cancer treatment: inhibition effects enhanced and side effects reduced, Colloids Surf. B 180 (2019) 110–117.
[31] C.W. Hsu, M.H. Hsieh, M.C. Xiao, Y.H. Chou, T.H. Wang, W.H. Chiang, pH-responsive polymeric micelles self-assembled from benzoic-imine-containing alkyl-modified PEGylated chitosan for delivery of amphiphilic drugs, Int. J. Biol. Macromol. 163 (2020) 1106–1116.
[32] C.C. Cheng, J.J. Huang, A.A. Muhable, Z.S. Liao, S.Y. Huang, S.C. Lee, C.W. Chiu, D.J. Lee, Supramolecular fluorescent nanoparticles functionalized with controllable physical properties and temperature-responsive release behaviour, Polym. Chem. 8 (2017) 2292–2298.
[33] J. Li, X. Meng, J. Deng, D. Lu, X. Zhang, Y. Chen, J. Zhu, A. Fan, D. Ding, D. Kong, Z. Wang, Y. Zhao, Multifunctional micelles dually responsive to hypoxia and singlet oxygen: enhanced photodynamic therapy via interactively triggered photosensitizer delivery, ACS Appl. Mater. Interfaces 10 (2018) 17117–17128.
[34] M. Tian, H. Tan, H. Li, C. You, Molecular weight dependence of structure and properties of chitosan oligomers, RSC Adv. 5 (2015) 69445–69452.
[35] W. Huang, C. Zhang, Tuning the size of poly(lactic-co-glycolic acid) (PLGA) nanoparticles fabricated by nanoprecipitation, Biotechnol. J. 13 (2018), https://doi.org/10.1002/biot.201700203.
[36] D. Saha, S. Kumar, D. Ray, J. Mata, V.K. Aswal, Structure and stability of biodegradable polymer nanoparticles in electrolyte solution, Mater. Lett. X 10 (2021), 100066.
[37] J.N. Zheng, H.G. Xie, W.T. Yu, X.D. Liu, W.Y. Xie, J. Zhu, X.J. Ma, Chitosan-g-MPEG-modified alginate/chitosan hydrogel microcapsules: a quantitative study of the effect of polymer architecture on the resistance to protein adsorption, Langmuir 26 (2010) 17156–17164.
[38] Y. Lin, Y. Yang, J. Yan, J. Chen, J. Cao, Y. Pu, L. Li, B. He, Redox/ATP switchable theranostic nanoparticles for real-time fluorescence monitoring of doxorubicin delivery, J. Mater. Chem. B 6 (2018) 2089–2103.
[39] N.S. Elbialy, N. Mohamed, Alginate-coated caseinate nanoparticles for doxorubicin delivery: preparation, characterisation, and in vivo assessment, Int. J. Biol. Macromol. 154 (2020) 114–122.
[40] D. Sprouse, Y. Jiang, J.E. Laaser, T.P. Lodge, T.M. Reineke, Tuning cationic block copolymer micelle size by pH and ionic strength, Biomacromolecules 17 (2016) 2849–2859.
[41] V.T.A. Nguyen, M.D. Pauw-Gillet, O. Sandre, M. Gauthier, Biocompatible polyion complex micelles synthesized from arborescent polymers, Langmuir 32 (2016) 13482–13492.
[42] H. Wen, H. Dong, J. Liu, A. Shen, Y. Li, D. Shi, Redox-mediated dissociation of PEG-polypeptide-based micelles for on-demand release of anticancer drugs, J. Mater. Chem. B 4 (2016) 7859–7869.
[43] W.H. Jian, T.W. Yu, C.J. Chen, W.C. Huang, H.C. Chiu, W.H. Chiang, Indocyanine green-encapsulated hybrid polymeric nanomicelles for photothermal cancer therapy, Langmuir 31 (2015) 6202–6210.
[44] H. Dou, M. Jiang, H. Peng, D. Chen, Y. Hong, pH-dependent self-assembly: micellization and micelle-hollow-sphere transition of cellulose-based copolymers, Angew. Chem. Int. Ed. 42 (2003) 1516–1519.
[45] W.H. Chiang, Y.H. Hsu, F.F. Tang, C.S. Chern, H.C. Chiu, Temperature/pH-induced morphological regulations of shell cross-linked graft copolymer assemblies, Polymer (51) (2010) 6248–6257.
[46] R. Biabanikhankahdani, S. Bayat, K.L. Ho, N.B.M. Alitheen, W.S. Tan, A simple add-and-display method for immobilisation of cancer drug on his-tagged virus-like nanoparticles for controlled drug delivery, Sci. Rep. 7 (2017) 5303.
[47] M.Y. Bai, S.L. Tang, M.H. Chuang, T.Y. Wang, P.D. Hong, Evaluation of chitosan derivative microparticles encapsulating superparamagnetic iron oxide and doxorubicin as a pH-sensitive delivery carrier in hepatic carcinoma treatment: an in vitro comparison study, Front. Pharmacol. 9 (2018) 1025.
[48] J. Lia, S. Ying, H. Ren, J. Dai, L. Zhang, L. Liang, Q. Wang, Q. Shen, J.W. Shen, Molecular dynamics study on the encapsulation and release of anti-cancer drug doxorubicin by chitosan, Int. J. Pharm. 580 (2020), 119241.
[49] B.R. Rajaganapathy, M.B. Chancellor, J. Nirmal, L. Dang, P. Tyagi, Bladder uptake of liposomes after intravesical administration occurs by endocytosis, PLoS ONE 10 (2015), e0122766.
[50] M. Ishii, Y. Fukuoka, S. Deguchi, H. Otake, T. Tanino, N. Nagai, Energy-dependent endocytosis is involved in the absorption of indomethacin nanoparticles in the small intestine, Int. J. Mol. Sci. 20 (2019) 476.
[51] X. Xu, Y. Li, H. Li, R. Liu, M. Sheng, B. He, Z. Gu, Smart nanovehicles based on pH-triggered disassembly of supramolecular peptide-amphiphiles for efficient intracellular drug delivery, Small 10 (2014) 1133–1140.
[52] Q. Feng, Y. Liu, J. Huang, K. Chen, J. Huang, K. Xiao, Uptake, distribution, clearance, and toxicity of iron oxide nanoparticles with diferent sizes and coatings, Sci. Rep. 8 (2018) 2082.